



1  
2  
3  
4  
5  
6  
7  
8  
9  
10  
11  
12  
13  
14  
15  
16  
17  
18  
19  
20  
21  
22  
23  
24  
25  
26  
27

## Supplementary Materials for

### Microbial Oxidation of Lithospheric Organic Carbon in Rapidly Eroding Tropical Mountain Soils

Jordon D. Hemingway, Robert G. Hilton, Niels Hovius, Timothy I. Eglinton, Negar Haghypour, Lukas Wacker, Meng-Chiang Chen, Valier V. Galy

correspondence to: [jordon\\_hemingway@fas.harvard.edu](mailto:jordon_hemingway@fas.harvard.edu)

#### **This PDF file includes:**

Materials and Methods  
Supplementary Text  
Figs. S1 to S6  
Captions for Tables S1 to S8  
References (35) – (65)

#### **Other Supplementary Materials for this manuscript includes the following:**

Tables S1 to S8

## 28 **Materials and Methods**

### 29 Sample collection

30 Taiwanese soil mineral (A+E) and saprolite (C) horizons were obtained as detailed in  
31 Ref. (35). In summary,  $\approx 0.5$  L was collected over 10 cm intervals, placed into sterile bags, dried  
32 at 80 °C, homogenized, and stored in the dark until analysis. LiWu River surface suspended  
33 sediment samples were collected at the Lushui gauging station (24.179° N; 121.492° E; 435 km<sup>2</sup>  
34 upstream catchment area; **Fig. S1**). Samples collected for this study span three successive  
35 typhoon events: Fung Wong (28 July – 4 August, 2008), Sinlaku (12 – 24 September, 2008), and  
36 Jangmi (28 September – 1 October, 2008). We include two additional samples collected at  
37 Lushui station: one during Typhoon Mindulle peak discharge (3 July 2004) as described in Ref.  
38 (36) and a second representing non-typhoon conditions (4 June 2008). Steep channels with high  
39 bed roughness and bedrock canyon walls result in well-mixed suspended sediments throughout  
40 the water column (37). We therefore assume that surface samples represent total exported  
41 suspended sediment.

42 For each sample, a known volume of water ( $\approx 0.5$  L) was collected into pre-rinsed HDPE  
43 bottles. Sediments were filtered through 0.22  $\mu$ m nylon membrane filters, transferred into petri  
44 dishes, dried at 60 °C, weighed, and stored in the dark until further analysis. Two samples  
45 collected during Typhoon Fung Wong peak discharge contained coarser lithic fragments that  
46 were separated and analyzed independently by sieving at 2 mm. Before further analysis,  $\geq 2$  mm  
47 fractions were rinsed with 3 % hydrogen peroxide at room temperature in a sonic bath to remove  
48 any fine-grained material from the surface of each rock fragment.

### 49 Bulk sample treatment

50 Bulk organic carbon (OC), <sup>13</sup>C contents, and <sup>14</sup>C contents have been reported previously  
51 for the sediment sample collected during Typhoon Mindulle peak discharge (17, 36) and all soils  
52 included in this study (35), with the exception of one saprolite (TS17) (**Table S1, S3**). Aliquots  
53 from all remaining samples were ground and homogenized using an agate mortar and pestle.  
54 Because Taiwan bedrock and suspended sediment samples contain significant amounts of detrital  
55 carbonate (17), de-carbonation was required. All samples were therefore acidified over 12 M  
56 HCl fumes (60 °C, 72 h) to remove carbonates (38). OC content was then determined on  
57 triplicate aliquots using a Fisons elemental analyzer. Total nitrogen content was determined  
58 similarly but using unacidified aliquots. Measurements were calibrated using a set of two  
59 primary standards (USGS-40 glutamic Acid, in-house glycine standard) and verified using two  
60 secondary standards (NBS-19 marble, in-house calcite standard) between every  $\approx 10 - 15$   
61 samples (38). Reported N/C represents the ratio of total nitrogen to acid insoluble OC. Bulk  
62 radiocarbon aliquots were acidified as described above, transferred into pre-combusted (850 °C,  
63 5 h) quartz tubes containing  $\approx 500$  mg CuO, evacuated, flame sealed, and combusted to CO<sub>2</sub>  
64 (850 °C, 5 h). Resulting CO<sub>2</sub> was further distilled and quantified manometrically. For a subset of  
65 soil and bedrock samples, bulk TiO<sub>2</sub> concentrations were measured on homogenized, un-ashed,  
66 and un-acidified aliquots by inductively coupled plasma optical emission spectrometry (ICP-  
67 OES) following Li-BO<sub>2</sub> alkali fusion at the Service d'Analyse des Roches et des Minéraux,  
68 INSU facility, Vandoeuvre-les-Nancy, France.

### 69 Ramped PyrOx analysis

70 Aliquots for Ramped PyrOx (RPO) were acidified as described above. Because residual  
71 chloride has been shown to interact with the RPO catalyst wire (39), acidified RPO aliquots were

72 rinsed 3× in 18.2 MΩ MilliQ water and freeze-dried overnight at -40 °C prior to analysis. To  
73 properly verify RPO <sup>14</sup>C mass balance, bulk OC and <sup>14</sup>C content was additionally determined on  
74 fumigated and rinsed aliquots for all samples in which RPO isotopes were measured. RPO  
75 analysis was performed as described previously (23, 39, 40) using ≈ 250 mg sample masses and  
76 an oven ramp rate of 5 °C min<sup>-1</sup>. Between each sample, CO<sub>2</sub> concentrations were calibrated using  
77 a 2-point calibration curve (pure He, 0 ppm CO<sub>2</sub>; in-house gas mixture, 465.5 ppm CO<sub>2</sub> in He)  
78 and a laboratory working standard (Nantucket mud patch) was additionally analyzed periodically  
79 to check temperature drift. All samples were binned into 3 to 7 fractions. Resulting CO<sub>2</sub> for each  
80 fraction was re-combusted with ≈ 100 mg CuO and ≈ 10 mg Ag pellets (525 °C, 1 h) to remove  
81 residual sulfur-containing gases (40) and was further distilled and quantified manometrically.

## 82 Fatty acid extraction, quantification, and purification

83 All soil and sediment samples with ≥ 2.5 g of remaining material were extracted for fatty  
84 acid analysis following the methods of Ref. (41). Samples were extracted in 20 mL of 9:1  
85 DCM:MeOH in a microwave-accelerated reaction system (CEM corporation) for 20 min at 100  
86 °C. Lipid extracts were then saponified using 0.5 M KOH in MeOH with ≈ 1 % 18.2 MΩ MilliQ  
87 water (70 °C, 2 h) to convert wax esters into carboxylic acids. Fifteen mL of MilliQ water was  
88 added and "base" fractions were liquid-liquid extracted in 5 mL hexane 5×. HCl was then added  
89 dropwise until pH 2 was reached and "acid" fractions were liquid-liquid extracted in 4:1  
90 hexane:DCM until the organic phase was clear (typically 5×). Both fractions were purified over  
91 1 g Supelclean amino-propyl silica gel (Supelco Analytical) using the following elution scheme:  
92 4 mL hexane (F1); 7 mL 4:1 hexane:DCM (F2); 10 mL 9:1 DCM:acetone (F3); and 14 mL 2 %  
93 formic acid in DCM (F4).

94 Acid and base fractions containing fatty acids (F4) were recombined and trans-esterified  
95 in 15 mL 95:5 MeOH:HCl (70 °C, 12 h) to produce fatty acid methyl esters (FAMES). Fifteen  
96 mL MilliQ water was then added and FAMES were liquid-liquid extracted into 4:1 hexane:DCM  
97 5× and further purified over 1 g amino-propyl silica gel eluted with 4 mL hexane (F4<sub>T</sub>F1) and 7  
98 mL 4:1 hexane:DCM (F4<sub>T</sub>F2). FAMES were then quantified using a Hewlett Packard 5890 gas  
99 chromatograph equipped with a flame ionization detector (GC-FID) and a Gerstel PTV injection  
100 system. Chromatographic separation was achieved using a VF-1ms capillary column (Agilent  
101 Technologies) and the following temperature program: ramp to 130 °C at 30 °C min<sup>-1</sup>; ramp to  
102 320 °C at 8 °C min<sup>-1</sup>; hold at 320 °C for 7.5 min. Samples were analyzed as single injections,  
103 quantified using an external standard (in-house FAMES mixture) injected at 3 concentrations  
104 between every 5 samples, and normalized to the extracted OC mass. Uncertainty was calculated  
105 using the standard deviation of the external calibration curve.

106 After quantification, unsaturated FAMES were removed using 0.5 g silver nitrate silica  
107 gel (Supelco Analytical) in a Pasteur pipette column eluted with 5 mL hexane (SN1) and 18 mL  
108 4:1 hexane:DCM (SN2). Saturated FAMES were contained in fraction F4<sub>T</sub>F2 SN2, which was  
109 split into two aliquots for <sup>13</sup>C/<sup>12</sup>C and <sup>14</sup>C/<sup>12</sup>C measurement. Individual FAMES homologues  
110 were separated for <sup>14</sup>C analysis using a preparatory column GC (PCGC) as described previously  
111 (42). Between 50 and 100 consecutive injections were made into either a Hewlett Packard 5890  
112 or an Agilent 7890 GC equipped with a RTX-1 column (Restek Corporation) and a 6-port  
113 Gerstel fraction collector with pre-combusted glass traps (450 °C, 4 h). Purified homologues  
114 were recovered into 4 mL DCM and further purified over 0.5 g silica gel activated with 1 % 18.2  
115 MΩ MilliQ water. Homologue purity was checked by injecting ≈ 1 % onto the GC-FID setup  
116 described above. Purified homologues were then transferred into pre-combusted quartz tubes

117 (850 °C, 5 h) containing  $\approx$  150 mg CuO, evacuated using a vacuum line, and oxidized to CO<sub>2</sub>  
118 (850 °C, 5 h). Resulting CO<sub>2</sub> was distilled and quantified manometrically.

### 119 Isotope measurement

120 All <sup>13</sup>C/<sup>12</sup>C ratios are reported in  $\delta^{13}\text{C}$  notation relative to Vienna Pee Dee Belemnite  
121 (VPDB). Bulk OC  $\delta^{13}\text{C}$  values were determined on triplicate acidified aliquots using the Fisons  
122 elemental analyzer described above and coupled to a Finnigan Delta<sup>plus</sup> isotope ratio mass  
123 spectrometer (IRMS) using a Finnigan-MAT Conflo II open split interface. Like % OC,  $\delta^{13}\text{C}$   
124 values were calibrated using two primary standards (USGS-40 glutamic Acid, in-house glycine  
125 standard) and verified using two secondary standards (NBS-19 marble, in-house calcite standard)  
126 between every  $\approx$  10 – 15 samples (38). Uncertainty is taken as the standard deviation of triplicate  
127 measurements. Saturated FAMES  $\delta^{13}\text{C}$  values were determined on triplicate injections using an  
128 Agilent 6890 GC coupled with the same Finnigan Delta<sup>plus</sup> IRMS operated with a GC/C  
129 combustion interface using O<sub>2</sub> trickle flow (43). Chromatographic separation was achieved using  
130 a CP-Sil 5CB capillary column (Agilent Technologies) and the following temperature program:  
131 ramp to 160 °C at 50 °C min<sup>-1</sup>; ramp to 340 °C at 6 °C min<sup>-1</sup>; hold at 340 °C for 28.5 min.  
132 Instrument drift was corrected using pulses of CO<sub>2</sub> with known isotope composition introduced  
133 between analyte peaks and  $\delta^{13}\text{C}$  values were further calibrated using a secondary in-house  
134 standard mixture injected between every 5 – 10 samples. Results were additionally corrected for  
135 the isotope composition of trans-esterification methanol. Uncertainty is taken as the standard  
136 deviation of triplicate injections combined with propagated error from the trans-esterification  
137 methanol isotope composition.

138 All <sup>14</sup>C/<sup>12</sup>C ratios are reported as fraction modern (Fm) relative to 95 % of the <sup>14</sup>C activity  
139 of NBS Oxalic Acid I in 1950 and are normalized to  $\delta^{13}\text{C} = -25 \text{‰}$  VPDB. We note that the Fm  
140 notation used here is thus identical to the F<sup>14</sup>C notation of Ref. (44). Fm values were determined  
141 either at the National Ocean Sciences Accelerator Mass Spectrometry (NOSAMS) facility  
142 following established graphitization methods (45, 46) or at ETH Zürich using a gas ion source  
143 coupled to a MIni radioCARbon DAting System (MICADAS) AMS (47). Results were corrected  
144 for procedural blank carbon contamination following Ref. (47) (bulk measurements), Ref. (39)  
145 (RPO), or Ref. (48) (FAMES). FAMES Fm values were additionally corrected for the isotope  
146 composition of trans-esterification methanol (48). Uncertainty is taken as a combination of that  
147 from analytical error, blank correction, and trans-esterification methanol correction (FAMES  
148 only).

149 Acidification is required for all samples in order to remove carbonates. However, small  
150 differences are observed between bulk % OC and Fm values measured following liquid HCl (35,  
151 36), fume HCl (this study), and fume HCl followed by rinsing (this study) acidification  
152 procedures. To assess the importance of these differences, we regress fumigated and rinsed Fm  
153 values vs. those generated after either liquid acid treatment or fumigation without rinsing. The  
154 resulting ordinary least squares regression slope is statistically identical to unity ( $r^2 = 0.988$ ;  $p$ -  
155 value =  $8.1 \times 10^{-15}$ ;  $n = 16$ ) with a regression root mean square error of 0.036 Fm units. To  
156 accurately compare our results to those of Refs. (35, 36), we retain liquid acid bulk Fm values  
157 where available (soils, Mindulle peak sediment) and use fumigated, non-rinsed values for  
158 samples initially presented in this study (TS17, 2008 sediments). Because results between  
159 different acid treatments are comparable to within 0.036 Fm units, our choice of acid treatment  
160 does not significantly impact our conclusions.

### 161 **Supplementary Text**

162 End-member mixing model

163 We use a two-end-member mixing model to estimate  $f_{ox}$ , the fraction of initial OC  
 164 contained in exhumed bedrock that is oxidized during soil formation. The total OC content  
 165 within a given soil sample,  $\% OC_{soil}$ , is defined as the sum of biospheric and petrogenic  
 166 contributions:

$$167 \quad \% OC_{soil} = \% OC_{bio} + \% OC_{petro}. \quad (S1)$$

168 We then write  $Fm_{soil}$ , the total  $^{14}C$  content of a given soil sample, as a weighted average of  $Fm$   
 169 values corresponding to  $OC_{bio}$  and  $OC_{petro}$ :

$$170 \quad (Fm_{soil})(\% OC_{soil}) = (Fm_{bio})(\% OC_{bio}) + (Fm_{petro})(\% OC_{petro}). \quad (S2)$$

171 Because bedrock is formed on timescales that are orders of magnitude longer than the  $^{14}C$  half-  
 172 life, petrogenic OC is  $^{14}C$ -free and  $Fm_{petro} = 0.0$  by definition. **Eq. S2** therefore simplifies to

$$173 \quad (Fm_{soil})(\% OC_{soil}) = (Fm_{bio})(\% OC_{bio}). \quad (S3)$$

174 We rearrange **Eq. S1** to solve for  $\% OC_{bio}$  and substitute into **Eq. S3** to yield

$$175 \quad (Fm_{soil})(\% OC_{soil}) = (Fm_{bio})(\% OC_{soil} - \% OC_{petro}). \quad (S4)$$

176 Because  $OC_{bio}$  addition will increase  $\% OC_{soil}$  relative to bedrock while  $OC_{petro}$  oxidation will  
 177 result in the opposite trend, our aim is to directly compare the OC content within soil samples to  
 178 that of the bedrock immediately below. We therefore define

$$179 \quad \Delta\%OC = \% OC_{soil} - \% OC_{bedrock}, \quad (S5)$$

180 where  $\% OC_{bedrock}$  is the petrogenic OC content of bedrock immediately underlying the soil  
 181 sequence. We rearrange **Eq. S5** to solve for  $\% OC_{soil}$  and substitute into **Eq. S4** to yield

$$182 \quad (Fm_{soil})(\Delta\%OC + \% OC_{bedrock}) = (Fm_{bio})(\Delta\%OC + \% OC_{bedrock} - \% OC_{petro}). \quad (S6)$$

183 Finally, we utilize the definition of  $f_{ox}$  to write the  $OC_{petro}$  content remaining in soil as the  
 184 fraction of initial bedrock OC that has not been oxidized:

$$185 \quad \% OC_{petro} = (1 - f_{ox})(\% OC_{bedrock}). \quad (S7)$$

186 Substituting **Eq. S7** into **Eq. S6** and rearranging, this becomes

$$187 \quad Fm_{soil} = Fm_{bio} \left[ \frac{\Delta\%OC + (f_{ox})(\% OC_{bedrock})}{\Delta\%OC + \% OC_{bedrock}} \right]. \quad (S8)$$

188 When plotting  $\Delta\%OC$  vs.  $Fm_{soil}$ , it can be seen that **Eq. S8** describes a hyperbola that asymptotes  
 189 to  $Fm_{bio}$  at high values of  $\Delta\%OC$  and contains curvature that is defined by  $f_{ox}$  and  $\% OC_{bedrock}$ . If  
 190  $Fm_{soil}$ ,  $Fm_{bio}$ , and  $\Delta\%OC$  are known for a set of soil samples, then we can simultaneously  
 191 determine the  $f_{ox}$  and  $\% OC_{bedrock}$  values that best describes OC evolution during soil formation  
 192 by finding the best-fit solution to **Eq. S8**.

193 We use measured  $Fm_{soil}$  and  $\% OC_{soil}$  for each sample and calculate  $\Delta\%OC$  using the OC  
 194 content for paired bedrock underlying a given soil sequence. Paired bedrock samples are not  
 195 available for some locations, in which case we estimate  $\Delta\%OC$  using bedrock formation average  
 196 OC content reported in Ref. (17) (**Table S1**). By using the unique bedrock OC content for each  
 197 soil profile, our model predicts the average fraction of  $OC_{petro}$  oxidized ( $f_{ox}$ ) rather than the  
 198 absolute mass. Fractional loss is better suited for first-order processes such as OC decomposition  
 199 (23, 49), since absolute OC loss depends on initial concentration and is likely to vary between

200 bedrock formations. Still, to fit a single mixing trend for the entire sample set, our model  
201 requires the average  $F_{m_{bio}}$  value as an input (**Eq. S8**).

202 Because  $n$ -C<sub>24+</sub> fatty acids are produced exclusively by vascular plants [see Ref. (50) for  
203 review], we estimate  $F_{m_{bio}}$  as the mean  $F_m$  value of these compounds extracted from all A+E  
204 horizon soils ( $F_{m_{bio}} = 1.045 \pm 0.079$ ,  $\pm 1\sigma$ ; **Table S2**). Fatty acid concentrations and  $F_m$  values  
205 are positively correlated in our sample set (**Table S2, S6**). We therefore weight individual plant-  
206 wax  $F_m$  values by precision only (*i.e.* we ignore concentration) when estimating  $F_{m_{bio}}$ . This  
207 prevents any bias toward high  $F_m$  values and maximizes the  $F_{m_{bio}}$  range, resulting in a  
208 conservative estimate of  $f_{ox}$  uncertainty. Nonetheless, weighting by concentration results in a  
209 statistically identical mean  $F_{m_{bio}}$  value of  $1.053 \pm 0.063$  ( $\pm 1\sigma$ ; **Table S2**). We note that  $F_{m_{bio}}$   
210 may differ slightly from plant-wax fatty acid values due to biases in remineralization rates  
211 between compound classes (51). Still, our model requires that  $F_{m_{bio}}$  is near 1.03, the highest  
212 measured  $F_{m_{soil}}$  value, which is consistent with plant-wax fatty acid estimates.

213 We solve **Eq. S8** for  $f_{ox}$  and % OC<sub>bedrock</sub> using nonlinear orthogonal distance regression  
214 (ODR) (52) as implemented by the SciPy package in Python 3. This technique finds the solution  
215 that minimizes the orthogonal distance error between measured and predicted points and is thus  
216 well suited for regressions involving uncertainty in both  $x$  and  $y$  variables. The model presented  
217 here is best suited for describing OC<sub>petro</sub> oxidation because (i) it calculates fractional rather than  
218 absolute loss, (ii) mixing curvature is highly sensitive to changes in  $f_{ox}$ , and (iii) it does not  
219 require extrapolation. We incorporate  $F_{m_{bio}}$ ,  $F_{m_{soil}}$ , and  $\Delta\%OC$  uncertainty into our model  
220 solution using a Monte Carlo resampling approach with 10,000 iterations. All distributions are  
221 assumed to be Gaussian, with a standard deviation for  $F_{m_{bio}}$  of 0.079, equal to that of plant-wax  
222 fatty acids (**Table S2**), and a standard deviation for each  $F_{m_{soil}}$  and  $\Delta\%OC$  value equal to its  
223 measurement uncertainty (**Table S1**). This approach results in a best-fit  $f_{ox}$  value of  $0.67 \pm 0.11$   
224 and a best-fit % OC<sub>bedrock</sub> value of  $0.30 \pm 0.10$  %, both of which are approximately normally  
225 distributed. Calculated % OC<sub>bedrock</sub> is statistically identical to the average bedrock OC contents  
226 underlying our soil sample set ( $0.36 \pm 0.16$  %,  $\pm 1\sigma$ ; **Table S1**), providing further confidence to  
227 the ability of this mixing model to accurately constrain OC<sub>petro</sub> oxidation.

228 We assess the possibility that our results are impacted by element mobility during  
229 weathering, which could artificially impact measured % OC values by removing mobile  
230 elements and thus increasing OC weight percent. To do so, we normalize % OC to the  
231 concentration of the immobile element titanium. That is, we define

$$232 \quad \omega_i = \frac{\%OC_i}{[TiO_2]_i}, \quad (S10)$$

233 where  $i$  represents either soil or bedrock and  $[TiO_2]$  is the measured titanium concentration as  
234 titanium dioxide. We then solve the model as described above after replacing each % OC value  
235 in **Eq. S8** by the corresponding  $\omega$  value.  $[TiO_2]$  data are not available for our entire sample set,  
236 and we thus limit this comparison to a single soil profile (samples TS1 – TS3 and TBR1; **Table**  
237 **S1**; **Fig. S2**). Resulting  $f_{ox}$  for this profile using titanium-normalized % OC data is  $0.72 \pm 0.06$ ,  
238 statistically identical to that calculated for the same samples using un-normalized data ( $0.71 \pm$   
239  $0.06$ ) as well as to the value reported above for the entire sample set ( $0.67 \pm 0.11$ ). We therefore  
240 conclude that loss of mobile elements has only a negligible effect on our calculated  $f_{ox}$  estimate.  
241 This result is consistent with the observed low chemical weathering intensity in the Central  
242 Range (18), thereby limiting the loss of mobile elements in soils.

243  
244 CO<sub>2</sub> flux estimate

245 We use  $f_{\text{ox}}$  to estimate  $\Phi_{\text{ox}}$ , the average CO<sub>2</sub> emissions flux due to OC<sub>petro</sub> oxidation in  
 246 soils across the Central Range. This relationship can be written as

$$247 \Phi_{\text{ox}} = \frac{(f_{\text{ox}})(\% \text{OC}_{\text{bedrock}})(\rho_{\text{soil}})(z_{\text{soil}})}{\tau_{\text{soil}}}, \quad (S11)$$

248 where  $\rho_{\text{soil}}$  is the soil density (t m<sup>-3</sup>),  $z_{\text{soil}}$  is the soil thickness (m) (15),  $\tau_{\text{soil}}$  is the soil residence  
 249 time on hillslopes (yr), and  $\Phi_{\text{ox}}$  has units of t C km<sup>-2</sup> yr<sup>-1</sup>. **Eq. S11** describes a steady-state  
 250 solution and implicitly assumes that average hillslope soil thickness is constant through time.  
 251 Because direct soil formation rate measurements are not available, we constrain a range of  
 252 possible  $\tau_{\text{soil}}$  values using three independent approaches:

253 (i) Landslide rates. Landslide depth in the Central Range is typically deeper than that of the  
 254 weathering front (53). Thus, the average time between landslides constrains a timescale over  
 255 which hillslope soils are refreshed. We compile measured landslide rates for four Central Range  
 256 catchments in which data are available (53-57). Landslide rates are known to increase after  
 257 extreme tectonic and climatic triggers that are typically described by centennial return times (28).  
 258 To provide a baseline landslide-driven  $\tau_{\text{soil}}$  range, and thus a conservative estimate of  $\Phi_{\text{ox}}$ , we  
 259 omit landslides immediately following the 1999 Chi Chi Earthquake and 2009 Typhoon Morakot  
 260 from our analysis. This results in an average of 0.14 to 1.62 % of catchment area affected by  
 261 landslides each year (**Table S8**). Inverting this rate yields an average  $\tau_{\text{soil}}$  value for the whole  
 262 landscape of 62 to 711 yr.

263 (ii) Denudation rates. Catchment-averaged denudation rates, termed  $\epsilon$ , have been estimated to be  
 264 3 to 6 mm yr<sup>-1</sup> across the Central Range on decadal to million-year (Myr) timescales (10).  
 265 Assuming that soil formation is a steady-state, continuous process, we then calculate

$$266 \tau_{\text{soil}} = \frac{z_{\text{soil}}}{\epsilon}. \quad (S12)$$

267 Because OC<sub>petro</sub> loss occurs within saprolites, we use measured C-horizon depths to constrain  $z_{\text{soil}}$   
 268 between 0.2 and 0.9 m (**Table S1**). Using these  $z_{\text{soil}}$  and  $\epsilon$  ranges, **Eq. S12** estimates a  $\tau_{\text{soil}}$  value  
 269 of 50 to 266 yr. This must be a minimum value of  $\tau_{\text{soil}}$ , as sediment-flux-based  $\epsilon$  calculations  
 270 include exported unweathered bedrock material from landslides (10). Such export will increase  $\epsilon$   
 271 by increasing fluvial sediment load but will not affect soil turnover times. We therefore treat  $\Phi_{\text{ox}}$   
 272 calculated using this method as a maximum value.

273 (iii) OC<sub>bio</sub> export flux. Assuming steady state conditions, we estimate soil turnover times as the  
 274 catchment-averaged biomass residence times according to

$$275 \tau_{\text{soil}} = \frac{M_{\text{bio}}}{\Phi_{\text{bio}}}, \quad (S13)$$

276 where  $M_{\text{bio}}$  is the total mass of OC<sub>bio</sub> on hillslopes (5000 to 9000 t OC<sub>bio</sub> km<sup>-2</sup>) (32) and  $\Phi_{\text{bio}}$  is  
 277 the fluvial OC<sub>bio</sub> export flux (11 to 31 t OC<sub>bio</sub> km<sup>-2</sup> yr<sup>-1</sup>) (32). Using these values, **Eq. S13**  
 278 estimates a  $\tau_{\text{soil}}$  range of 161 to 818 yr. The  $\Phi_{\text{bio}}$  estimate used in this calculation is conservative  
 279 (32) and inherently ignores any additional OC<sub>bio</sub> export processes other than fluvial transport.  
 280 This results in a minimum  $\Phi_{\text{bio}}$  value and a maximum  $\tau_{\text{soil}}$  estimate. We therefore treat  $\Phi_{\text{ox}}$   
 281 calculated using this method as a minimum value.

282 We use a Monte Carlo approach to solve **Eq. S11** and estimate  $\Phi_{\text{ox}}$  for each  $\tau_{\text{soil}}$  method.  
 283 Because input variables contain significant uncertainty and are described by unknown

284 probability density functions, we treat each as a uniform distribution across the range of possible  
285 values, with the exception of  $f_{\text{ox}}$  and % OC<sub>bedrock</sub>, for which we use the distributions calculated in  
286 the solution to **Eq. S8**, above. We then solve 10,000 iterations of **Eq. S11**. Results are therefore  
287 conservative and reported uncertainty is maximized. In addition to the  $\tau_{\text{soil}}$  ranges described  
288 above, inputted variable ranges are as follows: (i)  $f_{\text{ox}} = (0.52, 0.86)$ , 95% confidence interval for  
289 the model presented in this study; (ii) % OC<sub>bedrock</sub> = (0.17, 0.48), 95 % confidence interval for the  
290 model presented in this study; (iii)  $\rho_{\text{soil}} = (2.0, 2.5) \text{ t km}^{-3}$ , range of observed values (15); (iv)  $z_{\text{soil}}$   
291 = (0.2, 0.9) m, range of observed saprolite depths reported in Ref. (35). **Fig. S3A** shows the  
292 resulting  $\Phi_{\text{ox}}$  estimates for each  $\tau_{\text{soil}}$  method. Median values range from 6.1 to 18.6 t C km<sup>-2</sup> yr<sup>-1</sup>,  
293 statistically identical to catchment-integrated estimates using OC<sub>petro</sub> yield (19) and dissolved  
294 rhenium yield (5).

### 295 Ramped PyrOx

296 Measured RPO thermal profiles are a function of bond strength and OC chemical  
297 structure, but inherently depend on experimental conditions such as oven ramp rate. This  
298 dependency can be removed by treating OC decay as a function of  $E$ , the Arrhenius activation  
299 energy required to oxidize OC into CO<sub>2</sub> during RPO analysis.  $E$  is an intrinsic property of the  
300 chemical bonding environment experienced by each carbon atom and is therefore a suitable  
301 proxy for OC chemical composition (58). For each sample, we determine the underlying  $E$   
302 distribution that will lead to the observed thermal profiles, termed  $p(0,E)$ , following the  
303 distributed activation energy model of Ref. (23) (**Fig. 2A, S4**). This approach does not require  
304 any assumptions about the functional form of  $p(0,E)$  (e.g. Gaussian), but does require the  
305 Arrhenius pre-exponential factor,  $\omega$ , to be prescribed *a priori*. As recommended in Ref. (23), we  
306 choose  $\omega = 10^{10} \text{ s}^{-1}$  for all samples. Analyses were performed in the Python programming  
307 language v.3.5 using the open-source ‘rampedpyrox’ package (59) [see Ref. (23) for model  
308 details].

309 Our aim is to compare activation energy with <sup>14</sup>C content. We therefore calculate the  
310 temporal evolution of  $p(0,E)$  to determine the mean  $E$  value of OC that decays within each RPO  
311 fraction (23). The resulting  $E$  vs. Fm plot for all RPO fractions is shown in **Fig. 2B**. Some OC-  
312 rich A+E horizon samples contain a small amount of high- $E$  material with Fm values near 0.5. It  
313 has been shown previously that charring can occur within the RPO instrument due to free radical  
314 condensation during combustion (60) and results in an apparent shift toward higher  $E$  values for  
315 otherwise labile OC. This mechanism is the likeliest cause of observed high- $E$  material in A+E  
316 horizon samples. We interpret these fractions as a mixture of OC<sub>petro</sub> and thermally stabilized  
317 OC<sub>bio</sub> with Fm near 1.0 rather than representing a biospheric component that has pre-aged for  $\approx$   
318 6,000 <sup>14</sup>C yr. This interpretation is supported by plant-wax fatty acid Fm values, which preclude  
319 significant OC<sub>bio</sub> pre-aging (**Table S2**), and by the fact that these RPO fractions contain low  
320 carbon masses (**Table S5**). Thus, a small contribution by charred OC<sub>bio</sub> ( $\approx 5\%$ ) (60) can explain  
321 observed high- $E$  Fm values.

322 Because  $E$  is an intrinsic property of the bonding environment experienced by each  
323 carbon atom (23, 58), OC mixing has no effect on the end-member  $p(0,E)$  distributions. That is, a  
324 mixture of low- $E$  OC<sub>bio</sub> and high- $E$  OC<sub>petro</sub> cannot explain the presence of mid- $E$  material in  
325 saprolites. Rather, this requires a chemically unique OC source. To further interpret  $E$  vs. Fm  
326 relationships, we estimate the fraction of mid- $E$  material,  $f_{\text{mid}}$ , contained in each end member. We  
327 constrain  $f_{\text{mid}}$  for OC<sub>petro</sub> to be 0.04, the value for isolated  $\geq 2$  mm clasts from LiWu River  
328 sediment (sample LW3PETRO; **Table S4**). Similarly, we use high-OC surface soil samples

329 (TS5, TS18; **Table S4**) to determine that  $f_{\text{mid}} \leq 0.11$  for  $\text{OC}_{\text{bio}}$ . Because we have no direct  
 330 measurement of  $f_{\text{mid}}$  for chemically altered  $\text{OC}_{\text{petro}}$ , we approximate it using saprolites. Sample  
 331 TS4 is described by  $F_m = 0.211 \pm 0.002$  (**Table S1**), is free of plant-wax fatty acids (**Table S6**),  
 332 and contains an  $f_{\text{mid}}$  value of 0.51 (**Table S4**), the highest observed in our sample set. We  
 333 therefore assume that TS4 represents a minimum value for this end member and we constrain  $f_{\text{mid}}$   
 334  $\geq 0.51$  for chemically altered  $\text{OC}_{\text{petro}}$ .

335 Calculated  $f_{\text{mid}}$  values inherently depend on the choice of mid- $E$  range. Although our  
 336 chosen mid- $E$  range is based on end-member samples, it remains possible that these  $E$  values do  
 337 not quantitatively separate OC end-member populations. We therefore test the sensitivity of our  
 338 results to the chosen mid- $E$  range by re-calculating  $f_{\text{mid}}$  for each sample and end member after  
 339 allowing the mid- $E$  cutoff values to vary by  $\pm 10 \text{ kJ mol}^{-1}$ . As shown in **Fig. S5**, individual  
 340 sample and end-member  $f_{\text{mid}}$  values are impacted by our choice of mid- $E$  range. However,  
 341 mixing trends are qualitatively robust to such changes. We therefore conclude that the mixing  
 342 trends described in **Fig. 3A** are insensitive to our choice of mid- $E$  range, but we emphasize  
 343 caution against quantitatively interpreting end-member fractional contributions to any given  
 344 sample using  $f_{\text{mid}}$ .

### 345 Fatty acid sources and mixing

346 Because  $n\text{-C}_{24+}$  fatty acids are vascular-plant biomarkers (50) while  $iso\text{-C}_{15}$  and  $anti\ iso\text{-C}_{15}$   
 347  $\text{C}_{15}$  fatty acids are produced exclusively by bacteria (25, 26, 61), we use fatty acid concentrations  
 348 and isotopes to further constrain OC source mixing. For each sample, we calculate the fraction of  
 349 total measured fatty acids that are microbial in origin according to

$$350 \quad f_{\text{microbial}} = \frac{[a/i\text{-C}_{15}]}{[a/i\text{-C}_{15}] + \Sigma\text{LC}_{24-34}}, \quad (S14)$$

351 where  $[a/i\text{-C}_{15}]$  is the sum of  $anti\ iso\text{-C}_{15}$  and  $iso\text{-C}_{15}$  concentrations, and

$$352 \quad \Sigma\text{LC}_{24-34} = [C_{24}] + [C_{26}] + [C_{28}] + [C_{30}] + [C_{32}] + [C_{34}] \quad (S15)$$

353 is the sum of plant-wax fatty acid concentrations (**Table S6**). We note that our calculated  $f_{\text{microbial}}$   
 354 ignores any potential contributions to  $a/i\text{-C}_{15}$  fatty acids by autotrophic bacteria. Although data  
 355 are limited, Ref. (61) report that aerobic, heterotrophic bacteria such as *Arthrobacter* sp. and  
 356 *Flavobacterium* sp. contain significantly higher concentrations of  $i\text{-C}_{15}$  fatty acid than any other  
 357 analyzed organism, thus supporting the use of  $a/i\text{-C}_{15}$  fatty acids as a proxy for heterotrophic  
 358 bacteria. Furthermore, our approach is insensitive to non-bacterial heterotrophs such as fungi, as  
 359 these organisms do not produce significant  $a/i\text{-C}_{15}$  fatty acids (25, 26, 61). We therefore treat our  
 360 calculated  $f_{\text{microbial}}$  as a minimum estimate of total heterotrophic biomass contributions.

361 We additionally calculate the average  $\delta^{13}\text{C}$  values for microbial ( $a/i\text{-C}_{15}$ ) and plant-wax  
 362 ( $\Sigma\text{LC}_{24-34}$ ) fatty acids as the concentration-weighted mean of each corresponding homologue,  
 363 including propagated uncertainty (**Table S7**). It has been shown that heterotrophic lipids reflect a  
 364 consistent, small ( $\leq 3 \text{ ‰}$ )  $^{13}\text{C}$  fractionation relative to substrate material (26), and  $a/i\text{-C}_{15}$   $^{13}\text{C}$   
 365 content can therefore be used to distinguish microbial carbon sources. Vegetation and bedrock  
 366  $\delta^{13}\text{C}$  values in the Central Range are overlapping and span a 10 ‰ range (17, 34) and thus cannot  
 367 be separated based on absolute values. Rather, we track microbial carbon sources by utilizing  
 368  $\delta^{13}\text{C}$  correlations between bulk OC,  $a/i\text{-C}_{15}$ , and  $\Sigma\text{LC}_{24-34}$  in both A+E and C horizons. If  
 369 vascular-plant OC were the sole source of substrate to microbes, then  $a/i\text{-C}_{15}$   $\delta^{13}\text{C}$  values should  
 370 track those of  $\Sigma\text{LC}_{24-34}$  fatty acids. However, **Fig. S6** shows that this is not observed in either

371 A+E or C horizon samples, thus requiring that microbes additionally utilize a secondary carbon  
372 source.

373

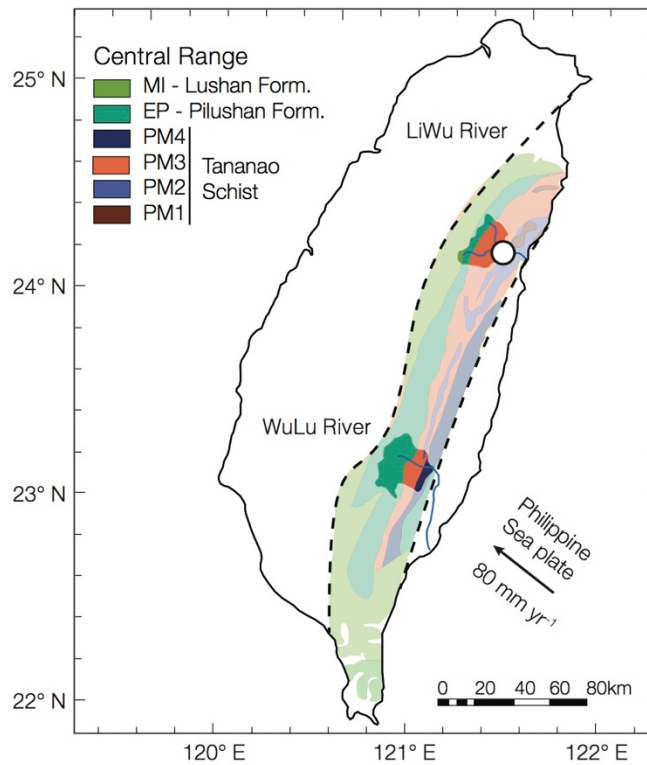
### 374 Net carbon budget

375 Finally, we compile carbon flux estimates from all relevant processes within Taiwanese  
376 rivers. For chemical weathering, we calculate CO<sub>2</sub> fluxes for the LiWu River in particular, as this  
377 is the only catchment in which cation/anion flux data have been published (18). To convert  
378 chemical weathering into CO<sub>2</sub> source/sink fluxes, we partition dissolved cations/anions into  
379 those derived from each rock type (silicate vs. carbonate) and weathering reaction (carbonic acid  
380 vs. sulfuric acid sourced from pyrite weathering). Using the data and approach of Ref. (18), we  
381 assume that all weathering-derived Na<sup>+</sup> and K<sup>+</sup> are sourced from silicate rocks. Using canonical  
382 silicate rock Ca<sup>2+</sup>/Na<sup>+</sup> and Mg<sup>2+</sup>/Na<sup>+</sup> ratios (0.35 and 0.24, respectively) (3) and calculating  
383 carbonate weathering by difference, this results in a cation charge flux of  $(8.7 \pm 0.2) \times 10^5$  mol  
384 km<sup>-2</sup> yr<sup>-1</sup> for silicate weathering and  $(8.8 \pm 0.2) \times 10^6$  mol km<sup>-2</sup> yr<sup>-1</sup> for carbonate weathering.

385 Furthermore, following Ref. (9), we assume that all weathering-derived SO<sub>4</sub><sup>2-</sup> is supplied  
386 from carbonate weathering by sulfuric acid. Ref. (62) estimate that  $(85 \pm 7)$  % of total dissolved  
387 SO<sub>4</sub><sup>2-</sup> in the Kaoping River, Southwest Taiwan, is derived from chemical weathering with the  
388 remainder due to anthropogenic inputs. This is likely an underestimate for the LiWu River, as the  
389 LiWu catchment is contained exclusively within a national park with limited farming and is thus  
390 less impacted by anthropogenic activity. Still, assuming this value is applicable and using the  
391 SO<sub>4</sub><sup>2-</sup> yield of Ref. (18), we estimate that  $(43 \pm 1)$  % of carbonate weathering is occurring *via*  
392 sulfuric acid.

393 It has been shown that carbon-cycle effect of chemical weathering depends on the  
394 timescale of interest (6). Because uplift of the Central Range began  $\sim 7.1 \pm 1.3$  Ma (63), we  
395 focus on timescales longer than that of marine carbonate precipitation (10<sup>5</sup> to 10<sup>6</sup> yr). Fluxes  
396 calculated here are therefore applicable to long-term, secular atmospheric CO<sub>2</sub> concentration  
397 trends. While million-year timescale trends in OC<sub>bio</sub> burial and OC<sub>petro</sub> oxidation have not been  
398 measured directly, Central Range erosion rates have remained nearly constant over million-year,  
399 millennial, and decadal timescales (10). Thus, barring drastic shifts in soil OC stocks or bedrock  
400 OC content since Central Range uplift, we assume that OC<sub>bio</sub> burial and OC<sub>petro</sub> oxidation fluxes  
401 are directly comparable to the long-term chemical weathering fluxes calculated here. Following  
402 Ref. (6), we convert cation fluxes into CO<sub>2</sub> source/sink fluxes as: (i) carbonate weathering by  
403 carbonic acid, no effect; (ii) carbonate weathering by sulfuric acid, 0.5 mol CO<sub>2</sub> produced per  
404 mol cation charge; (iii) silicate weathering by carbonic acid 0.5 mol CO<sub>2</sub> consumed per mol  
405 cation charge. We further adjust the silicate weathering flux to account for cation exchange in  
406 sediments and/or oceanic crust following Ref. (64). Resulting CO<sub>2</sub> flux estimates due to  
407 chemical weathering, OC<sub>petro</sub> oxidation [this study, Refs. (5, 19)], and OC<sub>bio</sub> burial in marine  
408 sediments (32) are shown in **Fig. S3**.

409

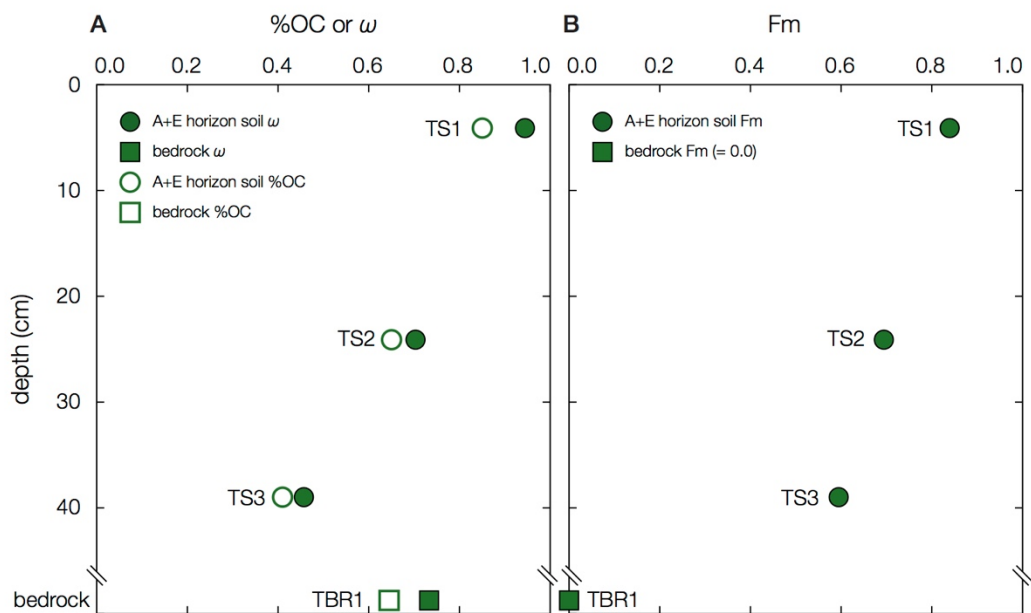


410

411 **Fig. S1.**

412 **Study site.** Taiwan map highlighting the Central Range formations: Lushan formation (MI;  
 413 green), Pilushan formation (EP; teal), and Tananao schist (blue, orange, purple, and red) (16).  
 414 LiWu and WuLu catchment colors are bolded, and LiWu suspended sediment sampling location  
 415 is shown as a white circle. See Ref. (35) for soil sample locations. Direction of Philippine Sea  
 416 Plate tectonic motion is shown as a black arrow (65).

417



418

419

**Fig. S2.**

420

**Representative soil depth profile.** (A) Organic carbon content, either as raw % OC or as [TiO<sub>2</sub>]

421

normalized  $\omega$  (Eq. S10), and (B) Fm for a single soil profile plotted against sampling depth (note

422

that TBR1 Fm value was not measured and is equal to 0.0 by definition). Circles are A+E

423

horizon soils and squares are underlying bedrock values (note the axis break since the exact

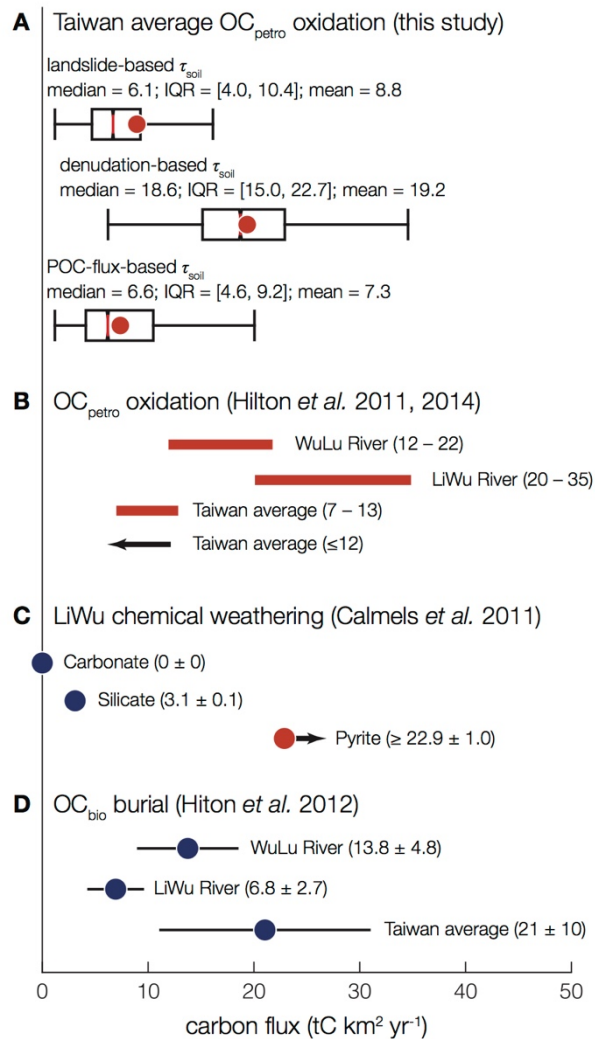
424

depth to bedrock is unknown). Individual sample IDs as described in **Table S1** are also plotted

425

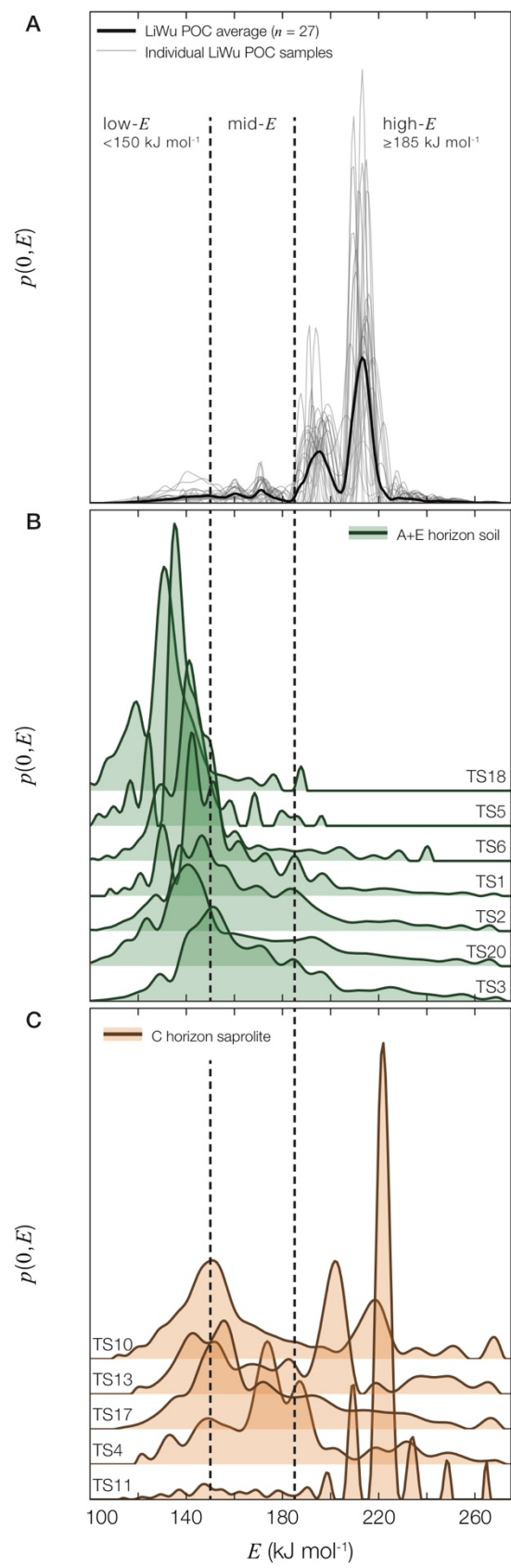
beside each point.

426

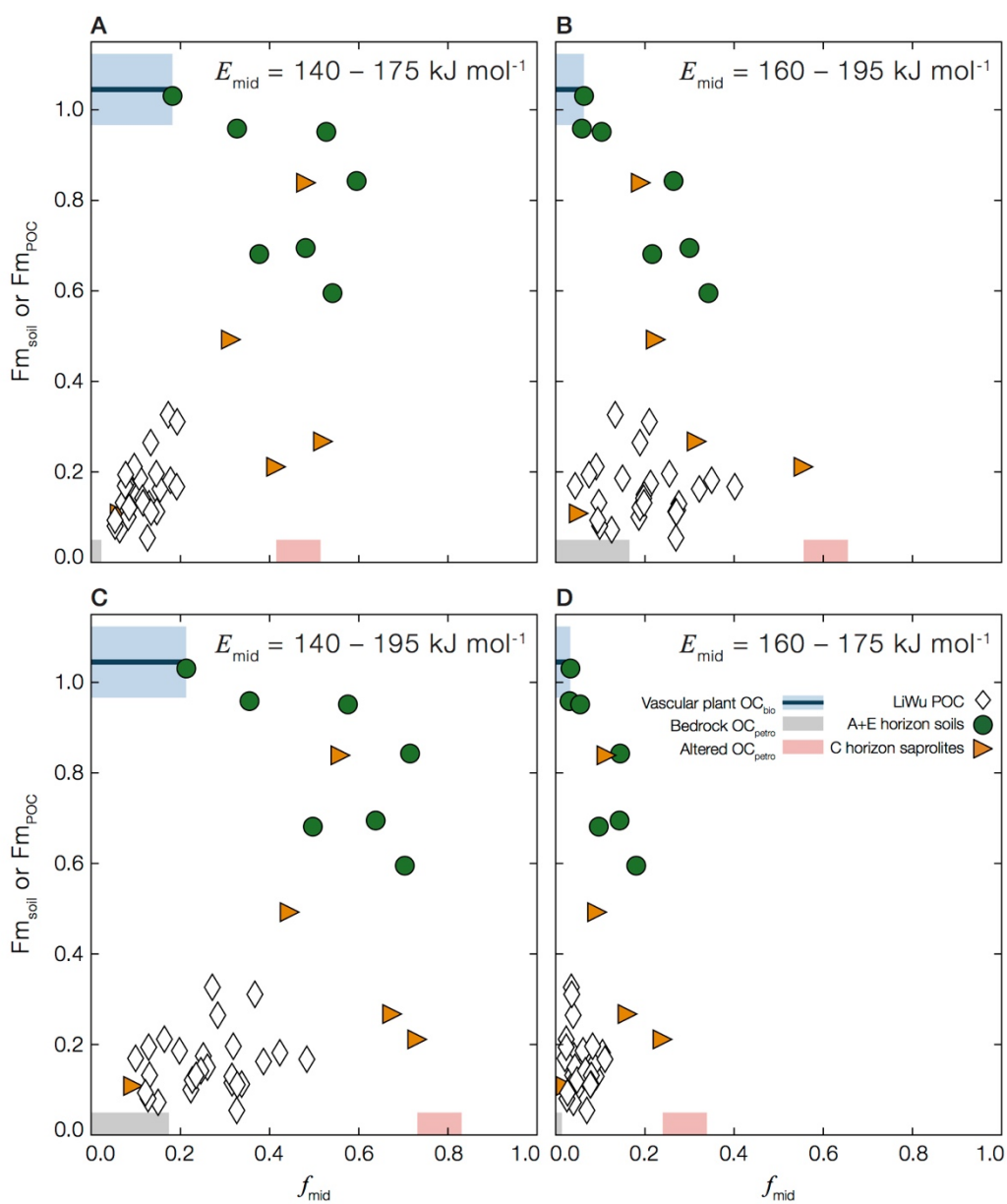


427

428 **Fig. S3.**  
 429 **Central Range CO<sub>2</sub> source/sink flux estimates.** (A) CO<sub>2</sub> emission flux due to  $OC_{\text{petro}}$  oxidation  
 430 in soils calculated in this study using three independent estimates of soil residence time ( $\tau_{\text{soil}}$ ).  
 431 Ranges are represented as box plots (IQR = interquartile range = 25<sup>th</sup> to 75<sup>th</sup> percentile) and  
 432 mean values are plotted as red circles. (B) Catchment-integrated  $OC_{\text{petro}}$  oxidation estimates  
 433 using fluvial dissolved rhenium yield (red bars) (5) and fluvial  $OC_{\text{petro}}$  export (black arrow) (5).  
 434 (C) CO<sub>2</sub> consumption due to silicate/carbonate rock weathering and CO<sub>2</sub> emission due to pyrite  
 435 oxidation within the LiWu catchment as estimated following Refs. (6, 18) and reported as  $\mu \pm$   
 436  $1\sigma$ . (D) CO<sub>2</sub> consumption due to  $OC_{\text{bio}}$  export and burial (32), reported as  $\mu \pm 1\sigma$ . For all panels,  
 437 red indicates CO<sub>2</sub> source, blue indicates CO<sub>2</sub> sink, and arrows indicate maximum/minimum  
 438 estimate.  
 439



441 **Fig. S4.**  
442 **Activation energy distributions.** (A) RPO-derived  $E$  distributions, termed  $p(0,E)$ , for all LiWu  
443 River POC samples, including  $\geq 2$  mm clasts, as a proxy for bedrock  $OC_{\text{petro}}$  ( $n = 27$ ). Individual  
444 runs are plotted as thin gray lines, and the mean  $p(0,E)$  for all samples is plotted as a thick black  
445 line. (B)  $p(0,E)$  for all A+E horizon and (C) C horizon soil samples analyzed in this study. For  
446 all panels, dotted lines separate  $p(0,E)$  into low- $E$  ( $< 150 \text{ kJ mol}^{-1}$ ), mid- $E$  ( $150 \leq E < 185 \text{ kJ mol}^{-1}$ ), and high- $E$  ( $\geq 185 \text{ kJ mol}^{-1}$ ) regions. All  $p(0,E)$  distributions integrate to unity ( $y$ -axis units  
447 not shown). For panels (B) and (C), individual samples are labeled, staggered along the  $y$ -axis  
448 for visual clarity, and sorted by descending bulk  $F_m$  values (**Table S1**).  
449  
450



451

452 **Fig. S5.**

453  $f_{\text{mid}}$  sensitivity analysis. Bulk Fm vs. calculated  $f_{\text{mid}}$  mixing model results as described in the

454 main text and shown in **Fig. 3A** but using variable mid- $E$  ranges: (A) 140 – 175 kJ mol<sup>-1</sup>, (B) 160

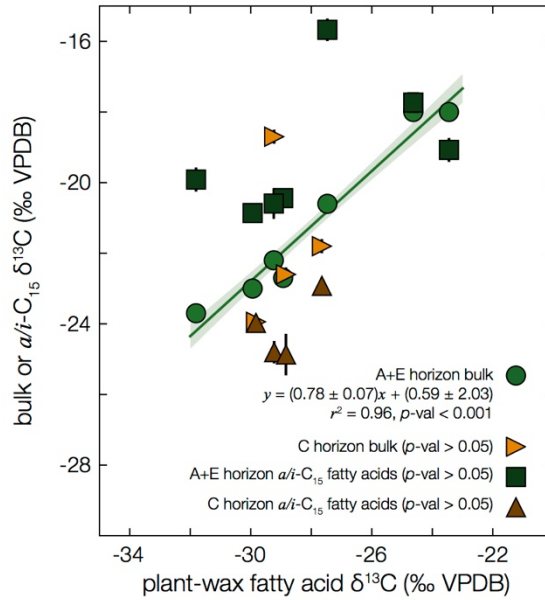
455 – 195 kJ mol<sup>-1</sup>, (C) 140 – 195 kJ mol<sup>-1</sup>, (D) 160 – 175 kJ mol<sup>-1</sup>. The calculated  $f_{\text{mid}}$  for each

456 sample and each end member does change as a function of mid- $E$  range. However, observed

457 mixing trends are qualitatively robust to such changes indicating that the choice of mid- $E$  range

458 has no significant effect on our interpretation. The legend printed in panel (D) applies to all

459 panels.



460

461 **Fig. S6.**

462 **Bulk and fatty acid  $\delta^{13}\text{C}$  correlations.** Plant wax fatty acid vs. bulk  $\delta^{13}\text{C}$  values for A+E (green  
 463 circles) and C (orange triangles) horizons, as well as plant wax fatty acid vs. microbial (*a/i-C<sub>15</sub>*)  
 464 fatty acid  $\delta^{13}\text{C}$  values for A+E (dark green squares) and C (dark orange triangles) horizons  
 465 (**Table S7**). All regressions were performed by weighted least squares. For visual clarity,  
 466 regression slopes,  $\pm 1\sigma$  uncertainty envelopes, equations, and  $r^2$  values are not shown for  
 467 relationships that are not statistically significant. Measurement error bars ( $\pm 1\sigma$ ) are plotted for all  
 468 samples but are sometimes smaller than marker sizes.

469

470 **Table S1.**  
471 Sample descriptions, bulk composition (%OC,  $\delta^{13}\text{C}$ , Fm,  $[\text{TiO}_2]$ ), and corresponding bedrock %  
472 OC and  $[\text{TiO}_2]$  for all soil samples used in this study, including results from two acid treatments  
473 for select samples.

474 **Table S2.**  
475 Fatty acid Fm values, including both the precision-weighted mean and std. dev. and the  
476 concentration-weighted mean and std. dev. for the sample set.

477 **Table S3.**  
478 Sample descriptions and bulk OC composition (%OC, N/C,  $\delta^{13}\text{C}$ , Fm) for all LiWu River  
479 sediment samples used in this study, including results from two acid treatments for select  
480 samples.

481 **Table S4.**  
482 RPO-derived  $f_{\text{low}}$ ,  $f_{\text{mid}}$ , and  $f_{\text{high}}$  for all samples used in this study.

483 **Table S5.**  
484 RPO fraction temperature ranges, carbon masses ( $\mu\text{gC}$ ), Fm, and  $E$  values for all samples in  
485 which fraction isotopes were measured.

486 **Table S6.**  
487 Carbon-normalized fatty acid concentrations ( $\mu\text{g gOC}^{-1}$ ) and calculated  $f_{\text{microbial}}$  for all samples in  
488 which fatty acids were extracted.

489 **Table S7.**  
490 Fatty acid  $\delta^{13}\text{C}$  values, including the concentration-weighted  $\Sigma\text{LC}_{24-34}$  and  $\Sigma a, i\text{-C}_{15}$  averages for  
491 all soil samples in which fatty acids were extracted.

492 **Table S8.**  
493 Literature compilation of landslide rates and corresponding soil residence times for the Central  
494 Range.  
495

496 **References**

- 497 35. R. G. Hilton, A. J. West, A. Galy, N. Hovius, G. G. Roberts, Geomorphic control on the  $\delta^{15}\text{N}$   
 498 of mountain forests. *Biogeosciences*. **10**, 1693–1705 (2013).
- 499 36. R. G. Hilton, A. Galy, N. Hovius, M.-C. Chen, M.-J. Horng, H. Chen, Tropical-cyclone-  
 500 driven erosion of the terrestrial biosphere from mountains. *Nat. Geosci.* **1**, 759–762  
 501 (2008).
- 502 37. J. M. Turowski, N. Hovius, M.-L. Hsieh, D. Lague, M.-C. Chen, Distribution of erosion  
 503 across bedrock channels. *Earth Surf. Process. Landforms*. **33**, 353–363 (2008).
- 504 38. J. H. Whiteside, P. E. Olsen, T. I. Eglinton, B. Cornet, N. G. McDonald, P. Huber, Pangean  
 505 great lake paleoecology on the cusp of the end-Triassic extinction. *Palaeoceanogr.,*  
 506 *Palaeoclim., Palaeoecol.* **301**, 1–17 (2011).
- 507 39. J. D. Hemingway, V. V. Galy, A. R. Gagnon, K. E. Grant, S. Z. Rosengard, G. Soulet, P. K.  
 508 Zigah, A. P. McNichol, Assessing the blank carbon contribution, isotope mass balance,  
 509 and kinetic isotope fractionation of the ramped pyrolysis/oxidation instrument at  
 510 NOSAMS. *Radiocarbon*. **59**, 179–193 (2017).
- 511 40. B. E. Rosenheim, M. B. Day, E. Domack, H. Schrum, A. Benthien, J. M. Hayes, Antarctic  
 512 sediment chronology by programmed-temperature pyrolysis: Methodology and data  
 513 treatment. *Geochem. Geophys. Geosyst.* **9**, Q04005 (2008).
- 514 41. J. D. Hemingway, E. Schefuß, B. J. Dinga, H. Pryer, V. V. Galy, Multiple plant-wax  
 515 compounds record differential sources and ecosystem structure in large river catchments.  
 516 *Geochim. Cosmochim. Acta.* **184**, 20–40 (2016).
- 517 42. V. V. Galy, T. I. Eglinton, Protracted storage of biospheric carbon in the Ganges-  
 518 Brahmaputra basin. *Nat Geosci.* **4**, 843–847 (2011).
- 519 43. A. L. Sessions, Isotope-ratio detection for gas chromatography. *J. Sep. Sci.* **29**, 1946–1961  
 520 (2006).
- 521 44. P. J. Reimer, T. A. Brown, R. W. Reimer, Discussion: Reporting and calibration of post-  
 522 bomb  $^{14}\text{C}$  data. *Radiocarbon*. **46**, 1299–1304 (2004).
- 523 45. A. P. McNichol, G. A. Jones, D. L. Hutton, A. Gagnon, R. M. Key, The Rapid Preparation of  
 524 Seawater  $\Sigma\text{CO}_2$  for Radiocarbon Analysis at the National Ocean Sciences AMS Facility.  
 525 *Radiocarbon*. **36**, 237–246 (1994).
- 526 46. A. Pearson, A. P. McNichol, R. J. Schneider, K. F. von Reden, Y. Zheng, Microscale AMS  
 527  $^{14}\text{C}$  measurement at NOSAMS. *Radiocarbon*. **40**, 61–75 (1998).
- 528 47. C. P. McIntyre, L. Wacker, N. Haghypour, T. M. Blattmann, S. Fahrni, M. Usman, T. I.  
 529 Eglinton, H.-A. Sayno, Online  $^{13}\text{C}$  and  $^{14}\text{C}$  gas measurements by EA-IRMS-AMS at ETH  
 530 Zürich. *Radiocarbon* **59**, 893–903 (2017).
- 531 48. K. Fornace, “Late Quaternary climate variability and terrestrial carbon cycling in tropical  
 532 South America,” thesis, MIT/WHOI (2016).
- 533 49. B. P. Boudreau, B. R. Ruddick, On a reactive continuum representation of organic matter  
 534 diagenesis. *Am. J. Sci.* **291**, 507–538 (1991).
- 535 50. T. I. Eglinton, G. Eglinton, Molecular proxies for paleoclimatology. *Earth Planet. Sci. Lett.*  
 536 **275**, 1–16 (2008).
- 537 51. P. A. Meyers, R. Ishiwatari, Lacustrine organic geochemistry – An overview of indicators of  
 538 organic matter sources and diagenesis in lake sediments. *Org. Geochem.* **20**, 867–900  
 539 (1993).
- 540 52. D. M. Glover, W. J. Jenkins, S. C. Doney, “Least squares and regression techniques,  
 541 goodness of fit and tests, and nonlinear least squares techniques,” in *Modeling Methods*

- 542 *for Marine Science* (Cambridge University Press, New York, ed. 1, 2011), pp. 49–74.
- 543 53. G.-W. Lin, H. Chen, N. Hovius, M.-J. Horng, S. Dadson, P. Meunier, M. Lines, Effects of  
544 earthquake and cyclone sequencing on landsliding and fluvial sediment transfer in a  
545 mountain catchment. *Earth Surf. Process. Landforms*. **33**, 1354–1373 (2008).
- 546 54. J.-C. Chang, O. Slaymaker, Frequency and spatial distribution of landslides in a mountainous  
547 drainage basin: Western Foothills, Taiwan. *Catena*. **46**, 285–307 (2002).
- 548 55. K.-T. Chang, S.-H. Chiang, M.-L. Hsu, Modeling typhoon- and earthquake-induced  
549 landslides in a mountainous watershed using logistic regression. *Geomorphology*. **89**,  
550 335–347 (2007).
- 551 56. Y.-C. Chen, K.-T. Chang, Y.-J. Chiu, S.-M. Lau, H.-Y. Lee, Quantifying rainfall controls on  
552 catchment-scale landslide erosion in Taiwan. *Earth Surf. Process. Landforms*. **38**, 372–  
553 382 (2013).
- 554 57. Y.-C. Chen, K.-T. Chang, H.-Y. Lee, S.-H. Chiang, Average landslide erosion rate at the  
555 watershed scale in southern Taiwan estimated from magnitude and frequency of rainfall.  
556 *Geomorphology*. **228**, 756–764 (2015).
- 557 58. Y. Tang, J. K. Perry, P. D. Jenden, M. Schoell, Mathematical modeling of stable carbon  
558 isotope ratios in natural gases. *Geochim. Cosmochim. Acta*. **64**, 2637–2687 (2000).
- 559 59. J. D. Hemingway, *rampedpyrox*: Open-source tools for thermoanalytical data analysis, 2016-  
560 , <http://pypi.python.org/pypi/rampedpyrox>, DOI: 10.5281/zenodo.839815 (2017).
- 561 60. E. K. Williams, B. E. Rosenheim, A. P. McNichol, C. A. Masiello, Charring and non-  
562 additive chemical reactions during ramped pyrolysis: Applications to the characterization  
563 of sedimentary and soil organic material. *Org. Geochem*. **77**, 106–114 (2014).
- 564 61. L. Zelles, Phospholipid fatty acid profiles in selected members of soil microbial  
565 communities. *Chemosphere* **35**, 275–294 (1997).
- 566 62. A. Das, C.-H. Chung, C.-F. You, Disproportionately high rates of sulfide oxidation from  
567 mountainous river basins of Taiwan orogeny: Sulfur isotope evidence. *Geophys. Res.*  
568 *Lett.* **39**, L12404 (2012).
- 569 63. L. Mesalles, F. Mouthareau, M. Bernet, C.-P. Chang, A. T.-S. Lin, C. Fillon, X. Sengelen,  
570 From submarine continental accretion to arc-continent orogenic evolution: The thermal  
571 record in southern Taiwan. *Geology*. **42**, 907–910 (2014).
- 572 64. C. France-Lanord, L. A. Derry, Organic carbon burial forcing of the carbon cycle from  
573 Himalayan erosion. *Nature*. **390**, 65–67 (1997).
- 574 65. L. S. Teng, Geotectonic evolution of late Cenozoic arc-continent collision in Taiwan.  
575 *Tectonophysics*. **183**, 57–76 (1990).